

A single-input, single-output electromagnetically-transduced microresonator array

A B Sabater, A G Hunkler and J F Rhoads

School of Mechanical Engineering, Birck Nanotechnology Center and Ray W Herrick Laboratories, Purdue University, West Lafayette, IN, 47907, USA

E-mail: jfrhoads@purdue.edu

Received 13 November 2013, revised 28 January 2014

Accepted for publication 10 February 2014

Published 28 April 2014

Abstract

Resonant microsystems have found broad applicability in environmental and inertial sensing, signal filtering and timing applications. Despite this breadth in utility, a common constraint on these devices is throughput, or the total amount of information that they can process. In recent years, elastically-coupled arrays of microresonators have been used to increase the throughput in sensing contexts, but these arrays are often more complicated to design than their isolated counterparts, due to the potential for collective behaviors (such as vibration localization) to arise. An alternative solution to the throughput constraint is to use arrays of electromagnetically-transduced microresonators. These arrays can be designed such that the mechanical resonances are spaced far apart and the mechanical coupling between the microresonators is insignificant. Thus, when the entire array is actuated and sensed, a resonance in the electrical response can be directly correlated to a specific microresonator vibrating, as collective behaviors have been avoided. This work details the design, analysis and experimental characterization of an electromagnetically-transduced microresonator array in both low- and atmospheric-pressure environments, and demonstrates that the system could be used as a sensor in ambient conditions. While this device has direct application as a resonant-based sensor that requires only a single source and measurement system to track multiple resonances, with simple modification, this array could find uses in tunable oscillator and frequency multiplexing contexts.

Keywords: microresonator, array, coupling, electromagnetically-transduced

(Some figures may appear in colour only in the online journal)

1. Introduction

Resonant microsystems have found broad applicability in environmental and inertial sensing [1, 2], signal filtering and timing applications [3–6]. Despite this breadth in utility, these devices commonly suffer from throughput constraints, or limitations on the total amount of information that can be processed by the system. These constraints are largely attributable to the frequency response structure of such resonators, and the fact that the current device design paradigm typically exploits only a single-mode response, and thus a single resonance. One way of circumventing the throughput

constraint is to elastically-couple multiple microresonators together [7–16]. These arrays are more complicated to design than systems based on isolated microresonators, however, due to the potential for collective behaviors to arise [17–22]. While collective behaviors, such as vibration localization, could find applications in microresonator-based mass sensors, due to their inherent sensitivity to small changes in system parameters, the systems exhibiting such behaviors are also very sensitive to fabrication imperfections. This fact can only partially be mitigated with post-processing [23].

An alternative way to circumvent the aforementioned throughput constraint is to employ arrays of mechanically-

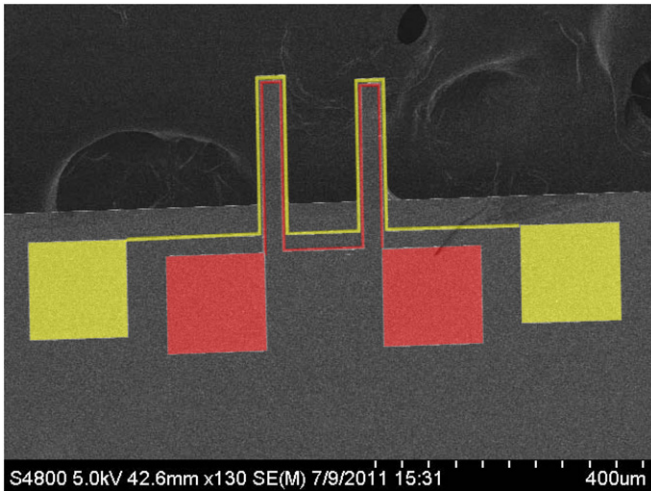


Figure 1. Representative scanning electron micrograph of an electromagnetically-transduced microresonator array. The device consists of two microcantilevers that share Au/Cr wires along the collective perimeter of the device.

uncoupled, electromagnetically-transduced microresonators [24–26], such as the one shown in figure 1. These devices exploit the interaction between a supplied current in a wire trace on a microresonator surface and an external magnetic field to produce a Lorentz force that is suitable for actuation. Since the device’s vibrations produce a time-varying magnetic flux within the circuit composed of the microresonator’s second wire trace, an induced electromotive force (EMF) is generated and can be used for sensing. The device of interest, shown in figure 1, consists of a microresonators array, wherein, the wire traces used for actuation and sensing follow the outer perimeter of the array. Due to the design of these wire traces, the entire array is actuated and sensed simultaneously. Since these microresonators are physically spaced, such that elastic coupling is negligible, and the lengths of the isolated microresonators are distinct, the electrical response of the array features resonances near the mechanical resonances of the isolated microresonators. Thus, this device has the advantage of being a single-input, single-output (SISO) system, yet also has multiple resonances that can be tailored to suit a specific application and an effective throughput that scales with number of constituent microresonators and/or resonances. Note that this device does not require signal multiplexing [27, 28] or a complicated measurement system [29] to track the multiple resonances. Also, note that though a similar device was developed by Venstra *et al* [30], the resonances of the device highlighted here are designed to be distinct and can be correlated to the vibration of a specific microresonator in the array. Though few devices have been shown to exhibit frequency responses akin to those subsequently detailed herein, notable examples are arrays of piezoelectric crystals [31] and optomechanically-transduced nanocantilevers [32].

2. Reduced-order modeling

A representative scanning electron micrograph of an electromagnetically-transduced microresonator array is shown

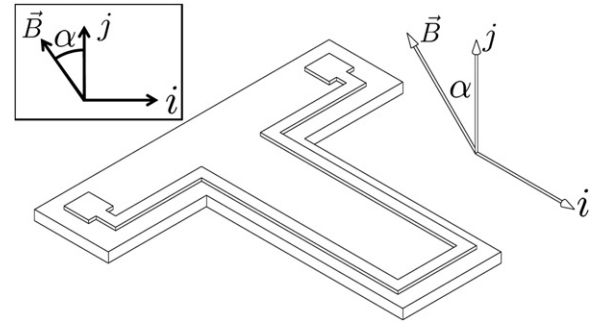


Figure 2. Schematic diagram of an isolated electromagnetically-transduced microresonator in three dimensions (from [26]). As shown in the inset, the magnetic field \vec{B} is oriented at an angle α with respect to the vertical reference. Note that only one of the two wire loops is depicted.

in figure 1. This device consists of two, frequency-mistuned microcantilevers (arrays with three microcantilever have been fabricated as well). In the following section, a brief derivation of a linear model for the response of this device is presented. A more detailed derivation that accounts for nonlinear phenomena, but is limited to an isolated microcantilever, can be found in a previous work [26]. It is worth noting that if the intended application of this device is to track the resonances of the array, the excitation can be limited such that nonlinear effects are insignificant.

As previously mentioned, the microcantilevers in the array shown in figure 1 are intentionally designed to have different lengths, or be frequency-mistuned, and are physically spaced so that the resulting elastic coupling is negligible. This results in the collective response of the device having resonances near the mechanical resonances of the isolated microcantilevers. Along the perimeter of these microcantilevers are two integrated Au/Cr wires. When the device is placed in a strong permanent magnetic field, oriented as shown in figure 2 [26], and a current is supplied to the outer wire, colored yellow, a Lorentz force is generated. Since the vibrations of the microcantilever array take place in a strong magnetic field, a time-varying magnetic flux is generated. As predicted by Faraday’s law, this time-varying magnetic flux produces an induced EMF, which can be used for sensing. This induced EMF is then measured as the potential between the two electrical contacts of the inner wire, colored red.

Assuming that the microcantilevers are physically spaced such that mechanical coupling effects can be ignored and the supplied current is small enough that nonlinear effects are trivial, the mechanical dynamics for the displacement $v(x, t)$, where x is the spatial variable referenced to the fixed end of the microcantilever and t is time, of an isolated microcantilever is governed by the Euler–Bernoulli beam equation

$$\rho A \ddot{v} + c \dot{v} + E I v'''' = F(t) \delta(x - l), \quad (1)$$

where ρ , A , c , E , I and l are the mass density, cross-sectional area, specific viscous damping coefficient, modulus of elasticity, cross-sectional moment of inertia and undeformed length, respectively, and (\bullet) and $(\bullet)'$ denote derivatives with respect to time t and the spatial variable x , respectively. Note that here the excitation is assumed to be a point load, modeled

with a delta function $\delta(x)$, located an infinitesimal distance from the tip of the microcantilever, such that the force does not need to be included in the boundary conditions. This force $F(t)$ is derived from the fundamental definition of the total Lorentz force along the width of the microcantilever

$$F(t) = gBi(t) \sin \alpha, \quad (2)$$

where g , B , $i(t)$ and α are the width of the microcantilever, the magnitude of the magnetic field strength, the supplied current and the orientation of the magnetic field, as defined in figure 2. Assuming ideal cantilever boundary conditions, the displacement of the microcantilever can be separated into two components related to the spatial and temporal components of the displacement

$$v(x, t) = \Psi(x)z(t). \quad (3)$$

Note that since the vibrations of interest are near the first bending mode of the microcantilever, a single-mode expansion is used, where $\Psi(x)$ is defined as

$$\Psi(x) = \cosh\left(\beta\frac{x}{l}\right) - \cos\left(\beta\frac{x}{l}\right) + \lambda \left[\sinh\left(\beta\frac{x}{l}\right) - \sin\left(\beta\frac{x}{l}\right) \right], \quad (4)$$

where β is the first solution to the transcendental equation

$$1 + \cos \beta \cosh \beta = 0, \quad (5)$$

and λ is

$$\lambda = \frac{\sin \beta - \sinh \beta}{\cos \beta + \cosh \beta}. \quad (6)$$

By substituting equation (3) into equation (1), multiplying by $\Psi(x)$, integrating over the length of the microcantilever, and scaling the result, an ordinary differential equation can be derived which governs the mechanical dynamics of the microcantilever

$$\ddot{z} + \frac{2\pi f_0}{Q}\dot{z} + 4\pi^2 f_0^2 z = \frac{2Bg \sin \alpha}{\rho Al} i(t), \quad (7)$$

where f_0 and Q are the undamped natural frequency and quality factor, respectively, and are defined as

$$f_0 = \frac{\beta^2}{2\pi} \sqrt{\frac{EI}{\rho Al^4}}, \quad (8)$$

$$Q = \frac{2\pi f_0 \rho A}{c}. \quad (9)$$

It is worth noting that $\Psi(x)$ has the properties that

$$\int_0^l \Psi^2(x) dx = l, \quad (10)$$

$$\int_0^l \Psi(x) \Psi'''(x) dx = \frac{\beta^4}{l^3}, \quad (11)$$

$$\int_0^l \Psi(x) \delta(x-l) dx = 2, \quad (12)$$

where the last integral relationship assumes that the delta function is defined such that it is entirely within the domain of $0 < x < l$.

To derive a model for the induced EMF, the magnetic flux of an isolated vibrating microcantilever must first be

considered. The magnetic flux $\Phi(t)$ due to the magnetic field \vec{B} that is in the neighborhood of the surface S of the microcantilever is defined as

$$\Phi(t) = \int_S \vec{B} \cdot \vec{n} dA, \quad (13)$$

where \vec{n} is the normal to the surface of the microcantilever. Ignoring nonlinear effects, this normal vector only has a component in the \mathbf{i} direction and has a magnitude of v' , since the angle of deflection is approximately equal to v' when displacements are small. Using the previous assumption that v can be separated in to spatial and temporal components, the magnetic flux of an isolated microcantilever is approximated as

$$\Phi(t) \approx 2Bg \sin \alpha z. \quad (14)$$

Using Faraday's law [33], which states the induced EMF in a closed circuit is equal to the opposite of the time derivative of the magnetic flux enclosed by this circuit, the induced EMF V_{EMF} of a single microcantilever is

$$V_{EMF} = -\frac{d\Phi(t)}{dt} \approx -2Bg \sin \alpha \dot{z}. \quad (15)$$

To broaden this result to an array of microcantilevers, the surface S can be extended to the entire array, yielding that the total induced EMF is the superposition of the isolated EMFs. Thus, the final governing equations for the array are

$$\ddot{z}_n + \frac{2\pi f_n}{Q_n} \dot{z}_n + 4\pi^2 f_n^2 z_n = \frac{2Bg \sin \alpha}{\rho Al_n} i(t), \quad \text{for } n = 1, \dots, N, \quad (16)$$

$$V_{EMF} = \sum_{n=1}^N -2Bg \sin \alpha \dot{z}_n, \quad (17)$$

where N is the number of microcantilevers in the array, l_n is the length of the n th microcantilever and f_n is the natural frequency of the n th microcantilever. Each microcantilever can also have a unique quality factor Q_n . While it is possible to set the quality factor for each microcantilever to match experiments, if it is assumed that each microcantilever has the same specific viscous damping coefficient, the quality factors are related by

$$Q_n = Q_0 \frac{l_0^2}{l_n^2}, \quad (18)$$

where Q_0 and l_0 are the quality factor and length of the shortest microcantilever, respectively.

As is often the case for microsystems, the measured potential is accompanied by parasitic effects that distort the measurable response from an ideal one. For this system, as was noted in a previous work [26], inductive and resistive coupling between the input and the output of the system are the primary causes for the measured potential, V_M , not being equal to the total induced EMF produced by the microcantilevers' motion, V_{EMF} . The circuit model shown in figure 3 was developed to aid in quantifying this relationship. The potential used to excite the device via the outer wire trace is denoted as V_{in} and supplies a current i_{in} . The Thévenin equivalent resistance of the source is R_S and is nominally 50 Ω . Note that in a previous work R_S was incorrectly reported as 10 k Ω [26]. The circuits composed of the probe station and the inner and outer wire traces are both

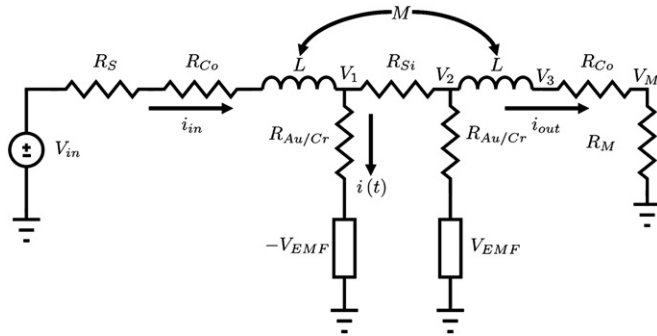


Figure 3. Equivalent circuit diagram used to model the electrical coupling between the input and output ports of the presented device. An excitation signal is provided by a voltage source V_{in} , which supplies a current i_{in} through the Thévenin equivalent resistor of the source R_S and a coaxial cable of resistance R_{Co} . The inner and outer wire loops are modeled as resistors $R_{Au/Cr}$ and the induced EMF is included as two current-controlled voltage sources. Note that the polarities of these sources are opposite due to the polarity of the inner and outer wire loops being opposite. To account for the conduction between the inner and outer wires, a lumped resistor R_{Si} is used. Effects related to inductive coupling are included with two inductors of self-inductance L and mutual inductance M . The resistor R_M is the input impedance of the lock-in amplifier used to acquire the measured voltage V_M . Note that R_{Si} is assumed to be much larger than $R_{Au/Cr}$ such that $i_{in} \approx i(t)$ and R_M is assumed to be much larger than R_{Co} such that $i_{out} \approx 0$. This diagram was presented in an earlier work [26] on an isolated microresonator, but can still be used for this particular device when the induced EMF is due to the entire ensemble of microresonators.

assumed to have self-inductances of L and a mutual inductance M between the two circuits. Note that while the probe station, the contact pads and the wire trace geometry contribute to the mutual inductance M , based on the magnitude of the observed inductive effects, the probe station and contact pads are the primary contributors to this effect.

Both of the wire traces used for actuation and sensing are assumed to have identical resistances $R_{Au/Cr}$. The induced EMF in the inner and outer wire trace circuits are modeled as current-controlled voltage sources. Note that the polarity of the sources are opposite due to the direction of current in each trace being opposite. To capture the conduction between the two circuits through the silicon substrate, a lumped resistance R_{Si} is used. This value is related to several sources of parasitic current, including the metal-semiconductor junctions formed by the contact pads and silicon substrate, which are assumed to be Ohmic contacts, and the finite resistivity of the silicon substrate. The input impedance of the lock-in amplifier R_M used to acquire the measured potential V_M is also included in the model. Note that nominally this input impedance is 10 M Ω .

Assuming that the self-inductance of the circuit with the outer wire trace is very small, R_{Si} is very large relative to $R_{Au/Cr}$ and that induced EMF is much smaller than the supplied voltage, it follows that $i_{in} \approx i(t)$ and that

$$i(t) = V_{in}/R, \quad (19)$$

$$V_1 = i(t)R_{Au/Cr}, \quad (20)$$

where $R = R_S + R_{Co} + R_{Au/Cr}$. Using Kirchoff's current law, under the assumption that R_M is much larger than R_{Co} such that $i_{out} \approx 0$,

$$\frac{V_1 - V_2}{R_{Si}} = \frac{V_2 - V_{EMF}}{R_{Au/Cr}}, \quad (21)$$

and the fundamental relationship for the induced EMF due to mutual inductance effects,

$$V_2 - V_M = M \frac{di(t)}{dt}, \quad (22)$$

an equation for the measured potential can be derived:

$$V_M = c_1 V_{EMF} + c_2 V_{in} - c_3 \dot{V}_{in}, \quad (23)$$

where

$$c_1 = \frac{R_{Si}}{R_{Si} + R_{Au/Cr}}, \quad (24)$$

$$c_2 = \frac{R_{Au/Cr}^2}{R(R_{Au/Cr} + R_{Si})}, \quad (25)$$

$$c_3 = \frac{M}{R}. \quad (26)$$

It is important to point out that M in equation (22) is a positive number and captures the fact that the direction of current in the inner and outer wires are in opposite directions. As noted earlier, the primary contributor to the mutual inductance is the probe station used for actuation and sensing, thus if the device was wire bonded, this inductance could be significantly reduced. While not obvious from equation (23), near a mechanical resonance there is destructive interference between the induced EMF and the potential due to resistive coupling effects. To combat this effect, the polarity of the measured potential can be reversed, which mathematically amounts to changing the signs of c_1 and c_3 . Note that the sign of c_2 does not change with the reverse polarity configuration. Due to the particularly small responses at atmospheric pressure, the reverse polarity configuration is used in all experimentally-recovered responses as it reduces the effects of antiresonances due to resistive coupling and helps improve the signal return. For clarity, the authors of this work are cognizant that polarity-dependent responses are abnormal, but polarity-dependent responses in integrated circuit transformers, which are very similar to the presented device, have been observed before [34, 35].

Using estimates of the dimensions and material properties for the microcantilever array, which are given in table 1, amplitude and phase responses of the measurable potential can be generated. Two different quality factors are used to model the device's response at different pressures. The low-pressure quality factor of 4800 and the atmospheric-pressure quality factor of 200 were selected to match experiments conducted at 75 μ Torr and 746 Torr, respectively. To demonstrate the differences between the standard and reverse polarity configurations, the low-pressure responses using the standard polarity configuration are shown in figure 4, while the low-pressure responses using the reverse polarity configuration are shown in figures 5 and 6. The atmospheric-pressure responses using the reverse polarity configuration are shown in figure 7. In all of the theoretical responses shown, an excitation voltage of 10 mV was used. To show the differences between the mechanical and electrical responses of the device, the mechanical frequency response functions of the

Table 1. Dimensions and material properties used to study the dynamic response of a representative electromagnetically-transduced microcantilever array. Based on these values, the natural frequencies of the array are expected to be approximately 66.72 kHz and 73.93 kHz at low pressure. The quality factors were chosen to match the experimental values obtained from frequency sweeps conducted within the two different pressure regimes.

Physical parameter	Value
Length of beam 1 (l_1)	200 μm
Length of beam 2 (l_2)	190 μm
Width (g)	50 μm
Thickness (v_0)	2 μm
Modulus of elasticity (E)	159 GPa
Mass density (ρ)	2330 kg m^{-3}
Quality factor at 75 μTorr (Q_0)	4800
Quality factor at atmospheric pressure (Q_0)	200
Magnetic field strength (B)	0.1 T
Magnetic field orientation (α)	$\pi/2$ rad
Au/Cr trace resistance ($R_{\text{Au/Cr}}$)	100 Ω
Lumped substrate resistance (R_{Si})	600 k Ω
Mutual inductance (M)	0.2 μH

microcantilevers are shown in red (short dashes) and blue (long dashes) and use the left vertical axis, while the electrical response is shown in black (solid curve) and uses the right vertical axis. For clarity, the mechanical frequency response is defined as the velocity of an isolated microcantilever, measured at its tip, normalized with respect to the excitation voltage.

As was discussed in [26], inductive and resistive coupling between the input and output of the device alters the response. This input/output coupling issue has been observed in other micro/nanosystems, including other electromagnetically-transduced microresonators [24], electrostatically-transduced resonators [36–39] and carbon nanotubes [40, 41], and is sometimes referred to as feedthrough or parasitic feedthrough. A common feature of systems with input/output coupling are antiresonances. Antiresonances can be observed in the response of this device, even when the device's output is only weakly inductively and resistively coupled to the input. This is due to destructive interference between the induced EMF and the parasitic signals. Antiresonances due to inductive coupling are independent of the polarity of the measured response, but antiresonances due to resistive coupling can be partially quenched by reversing the polarity of the measured response. Thus, as mentioned earlier, the reverse polarity configuration is used in all experimentally-recovered responses to mitigate the antiresonance effects.

Another effect related to input/output coupling is that the input voltage biases the response such that in frequency ranges where the mechanical response is trivial, the electrical response linearly scales with the input voltage. In addition to creating a qualitative difference between the mechanical and electrical response of the device, this also exacerbates issues related to noise. For the mechanical response, non-resonant noise contributions are significantly filtered. For the electrical response, however, input/output coupling allows some of the non-resonant noise contributions to be passed through to the output. This makes the recovered electrical response more

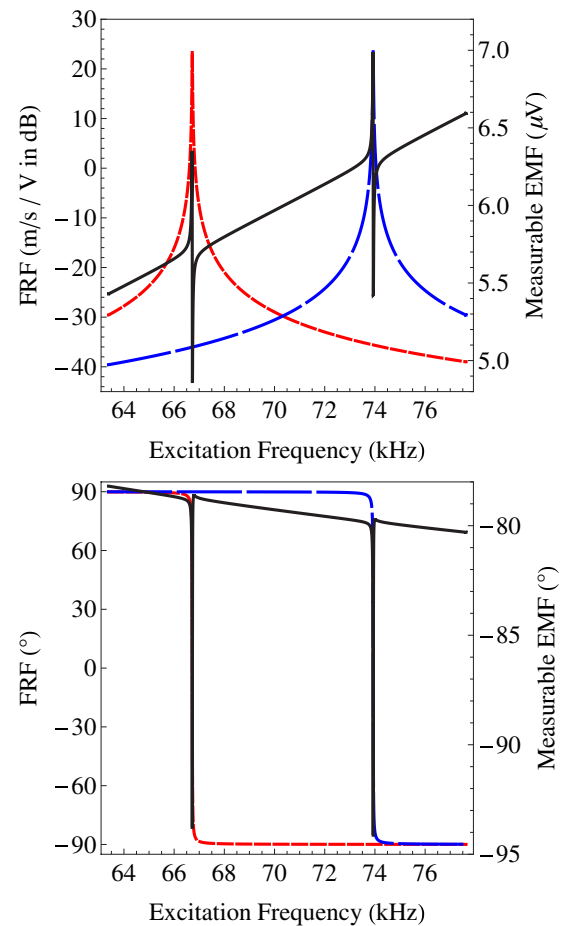


Figure 4. Theoretical amplitude and phase responses at 75 μTorr for an excitation of 10 mV obtained using the standard polarity configuration. Note that the mechanical responses of the device are shown in red (short dashes) and blue (long dashes) and use the left vertical axis, while the electrical response is shown in black (solid curve) and uses the right vertical axis. Due to inductive and resistive coupling effects between the input and output, there are antiresonances in the electrical response near mechanical resonances and the input voltage biases the response. Also, note that the non-resonant phase response is dominated by the parasitic inductive and resistive coupling between the input and output.

susceptible to noise from the excitation and measurement systems [39].

Inductive and resistive coupling also alter the phase response of the device such that the non-resonant phase is dictated by the particular form of input/output coupling. The phase response is also altered at resonance, which can lead to implementation issues if the device is intended to be used in a closed-loop system. Also note that in figure 4, which uses the standard polarity configuration, the non-resonant phase is close to -90° and that near a resonance, the phase tends to approach $\pm 180^\circ$, but in figure 5, which uses the reverse polarity configuration, the non-resonant phase is close to 90° and that near a resonance, the phase tends to approach 0° . In an experimental situation, these differences can be used to identify the polarity of the sensing circuit, if there is some ambiguity.

Lastly, it is important to note that input/output coupling causes the mechanical and electrical resonant frequencies to

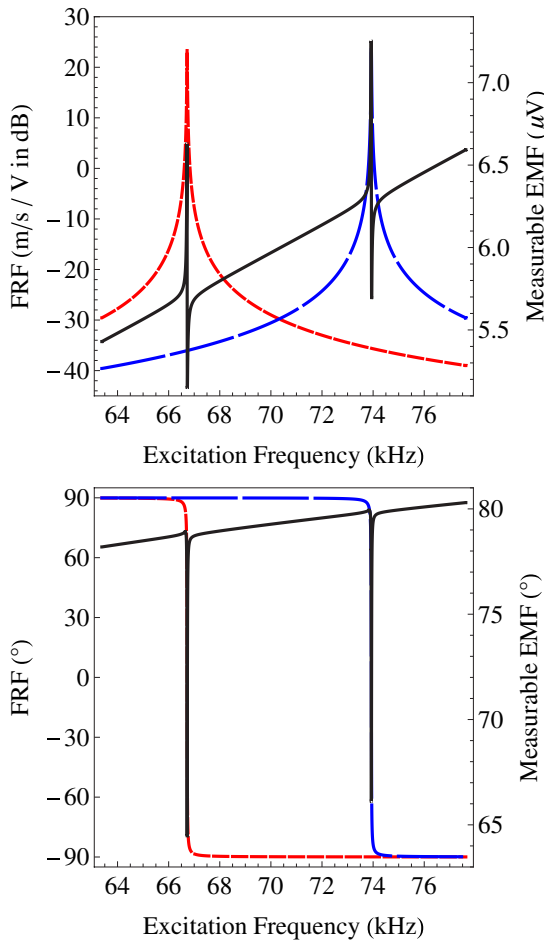


Figure 5. Theoretical amplitude and phase responses at 75 μ Torr for an excitation of 10 mV obtained using the reverse polarity configuration. The only difference between this case and the one shown in figure 4 is the polarity of the measurement, yet there are subtle differences in the responses. Antiresonance effects due to resistive coupling are smaller, thus the amplitude response close to a mechanical resonance is marginally greater than in figure 4. In addition, the non-resonant phase is approximately 180° out of phase with the non-resonant phase shown in figure 4 and the phase near a mechanical resonance tends to approach 0° instead of $\pm 180^\circ$.

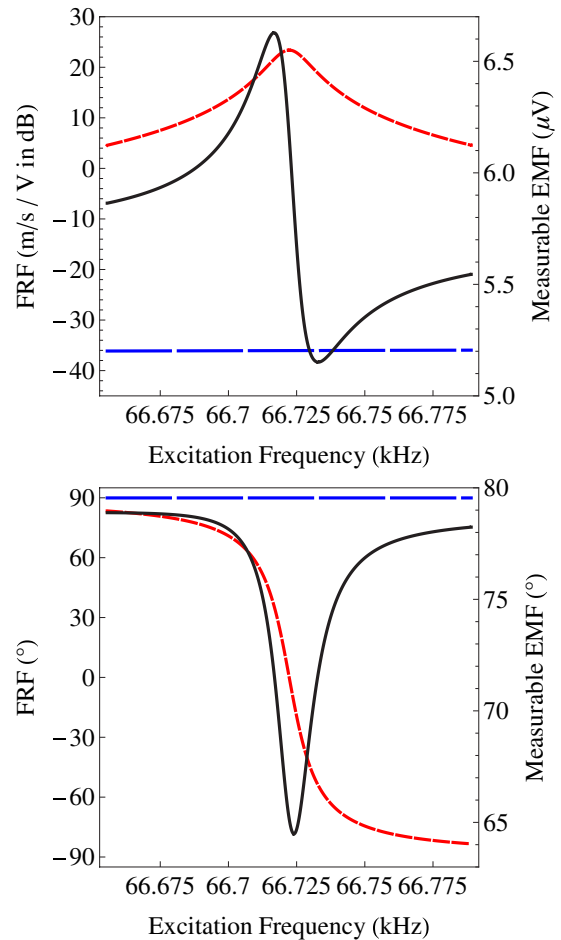


Figure 6. The same theoretical amplitude and phase responses as shown in figure 5, except over a smaller frequency range. Besides showing in detail the antiresonance and input voltage biasing caused by input/output coupling, these plots show that the mechanical and electrical resonant frequencies are distinct due to the same coupling.

be distinct, which might lead one to erroneously identify differences between the observed resonant frequencies and the designed resonant frequencies as being caused by fabrication imperfections. This effect is shown clearly in figure 6. In regards to the operation of the device at different pressures, changes in the response near a mechanical resonance are more dramatic at low pressure than at atmospheric pressure. Thus, when operating the device at atmospheric pressure, relatively small frequency increments near a mechanical resonance might be needed, as compared to a device that does not have input/output coupling issues, to resolve a response due to array vibrations.

3. Experimental results

To demonstrate the feasibility of a SISO device based on electromagnetic-transduction, devices were fabricated using silicon-on-insulator technology with a four step process, as

shown in figure 8, at the Birck Nanotechnology Center. In the first process, Au/Cr was deposited on the surface of the 10.16 cm, p-type, high resistivity (1000 Ω cm) wafer and selectively removed using photolithographic processes to form the wire traces and contact pads. Next, using reactive ion etching, the device layer of the wafer was etched to form the microcantilevers. To form the trenches that the microcantilevers vibrate in, deep reactive ion etching was used to etch the handle wafer from the bottom side. Finally, the microcantilevers were released from the silicon dioxide insulator layer using hydrofluoric acid. The device that was used to collect the results shown in this work, with the probes used for actuation and sensing on the device's contact pads, is depicted in figure 9. Due to issues with the wire traces being removed during the release process, not all of the silicon dioxide, false colored in figure 9 as purple, was removed. Note that the inner and outer wire traces are false colored as red and yellow, respectively, to be consistent with the convention used in figure 1. It is believed that the reason as to why the natural frequencies of the tested device do not more closely match the predicted ones is in part due to this residual silicon dioxide, as this residual decreases the effective length

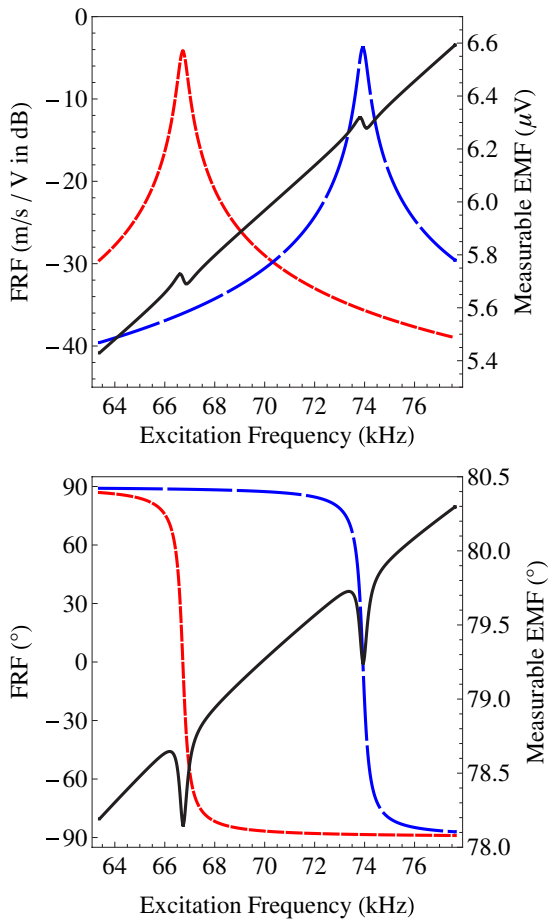


Figure 7. Theoretical amplitude and phase responses at atmospheric pressure (746 Torr) for an excitation of 10 mV obtained using the reverse polarity configuration. Due to the quality factor of the microresonators being much lower at atmospheric pressure, the electrical response due to the vibrations of the array is much smaller. Thus, when operating the device in this mode, the frequency increments used when performing frequency sweeps must be fine enough to capture the response near the resonances.

of the microcantilevers, which in turn increases their natural frequencies. One benefit of this residual silicon dioxide is that effects related to elastic coupling are further reduced as compared to a fully-released array.

It is important to note that as in any microstructure, these microcantilevers are susceptible to common fabrication issues, including poor photolithographic mask alignment, device layer variability, and over/underetching during structural release. In a previous work by the authors [26], a slightly thicker than reported (by the wafer supplier) device layer was identified as the reason why the experimentally-estimated natural frequencies were greater than the ones obtained from the model. Here, as noted above, there were issues related to device release. Despite these issues, since the microcantilevers in the array are physically spaced such that they are mechanically uncoupled, for the most part device imperfections have only a local effect. Thus, if a device is overetched such that ideal boundary conditions are not applicable, for example, the issue is isolated to that particular element in the array.

For the experiments described in this work, a grade N38SH sintered NdFeB slab magnet manufactured by Eclipse

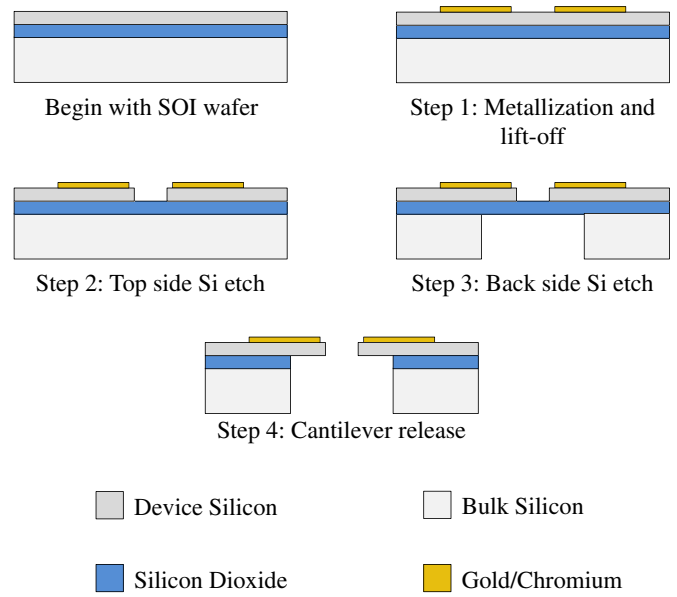


Figure 8. Fabrication process flow used to produce the electromagnetically-transduced microresonators [26].

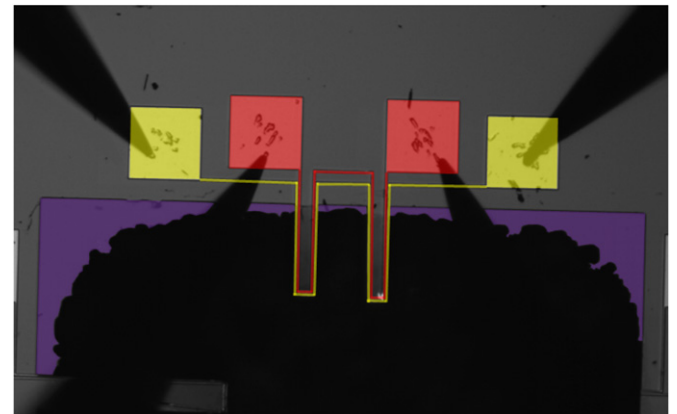


Figure 9. False-colored picture of the microcantilever array used to collect the presented results. The yellow region is the outer wire trace used for actuation, the red region is the inner wire trace used for sensing, and the purple region is residual silicon dioxide left over from device release. Due to issues with the Au/Cr traces being removed during release, the release time used was shorter than needed to fully remove all of the silicon dioxide.

Magnetics (model N317) and of dimensions 2.5 cm × 2.5 cm × 0.25 cm was used to generate the magnetic field. The remanence of these magnets range from 1.22–1.26 T, however, the magnetic field strength near the poles of the magnet is usually only 20%–50% of the remanence [42]. In order to maximize the component of the magnetic field used for transduction, the array was placed near the edge of the magnet, and the microcantilevers in the array were aligned such that the fixed end of the beams were parallel to the magnet’s edge. While this magnet and experimental setup facilitated experiments in a laboratory setting, portable applications would require either integrating magnetic material [42–47] or a solenoid [48–51]. Both methods have distinct advantages and pitfalls, but these relatively recent citations demonstrate that progress is being made and that it may be

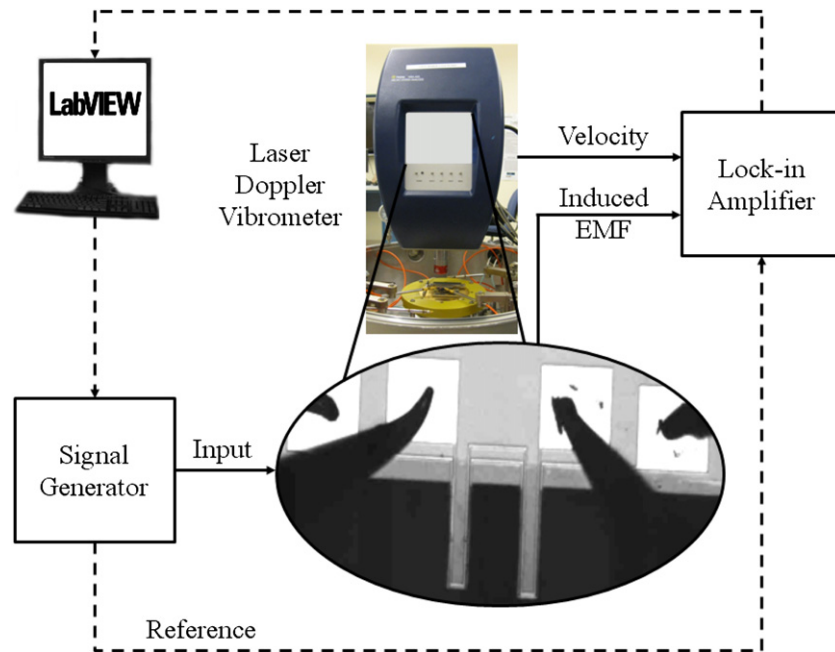


Figure 10. Block diagram of the experimental setup used to acquire both the mechanical and electrical responses of the electromagnetically-transduced microresonators array (from [26]). An Agilent 33220A arbitrary waveform generator was used as the source. Using an Agilent 8648D synthesized signal generator as an external reference, this source was controlled via LabView to perform frequency sweeps. A Polytec MSA-400 laser Doppler vibrometer was used to measure the velocity of the microcantilevers in the array and a Suss Microtec PLV-50 probe station enabled both transduction and pressure control. The devices were placed on a strong permanent magnet, in the chamber with a pressure of $75 \mu\text{Torr}$ for low-pressure testing and at 746 Torr for atmospheric-pressure testing. Both mechanical and electrical responses were measured using a Stanford Research Systems SR830 lock-in amplifier.

feasible to build complete miniature systems that use one of the arrays detailed in this work.

A block diagram of the experimental setup is shown in figure 10. Frequency sweeps are controlled by a LabView interface and the setup is capable of acquiring both mechanical and electrical responses. An Agilent 33220A arbitrary waveform generator was used as the source, however, due to issues with short-term frequency stability, an Agilent 8648D synthesized signal generator was used as an external reference. It is important to note that the Agilent 33220A was operated with a fixed output impedance of 50Ω . Transduction and pressure control was enabled by a Suss Microtec PLV-50 probe station. The velocity of the microcantilevers in the array was measured using a Polytec MSA-400 laser Doppler vibrometer and both amplitude and phase data from mechanical and electrical responses were recovered using a Stanford Research Systems SR830 lock-in amplifier. Due to differences in the response structure between mechanical and electrical measurements, a 3 ms time constant and 400 ms delay time were used for mechanical measurements and a 300 ms and 3 s delay time were used for electrical measurements. It is worth noting that in the mechanical responses, noise contributions at frequencies not close to a mechanical resonance are significantly filtered, but due to input/output coupling in the electrical responses, noise is only marginally filtered.

Figures 11–13 depict the experimentally-recovered responses of the device operated at both low pressure and atmospheric pressure. The results from low-pressure testing determined that the low-pressure resonant frequency of the microcantilever on the left in figure 9 was 77.449 kHz , while

for the microcantilever on the right it was 78.133 kHz . The associated quality factors were 4397 and 4797, respectively. In figure 11, and in the rest of the experimentally-recovered responses, mechanical frequency responses are shown in red (circles) and blue (crosses) for the left and right microcantilever, respectively, and electrical responses are shown in black (dots). Note that an excitation of 20 mVpp was used. As was discussed in the previous section, several effects related to inductive and resistive coupling are shown: antiresonances and response bias in the amplitude responses and the non-resonant phase response being dominated by parasitic effects. It is also worth noting that the mechanical responses show that any coupling between the microcantilevers, elastic or electrical, is negligible. Figure 12 shows the results of a different electrical response, which was collected under the same conditions, but over a smaller frequency range. This figure shows that the mechanical and electrical resonant frequencies are distinct due to inductive and resistive coupling effects.

Results from trials conducted at atmospheric pressure are shown in figure 13. The resonant frequencies of the left and right microcantilevers were 77.106 kHz and 77.776 kHz , respectively, with associated quality factors of 202 and 190, respectively. Note that since the excitation used in these trials was 100 mVpp , the magnitude of the measured signal was larger; however, due to the quality factors being smaller, the component of the response due to the vibration of the array is much smaller. This decrease in the component of the response due to array vibrations, besides qualitatively changing the response structure, necessitates in application an excitation

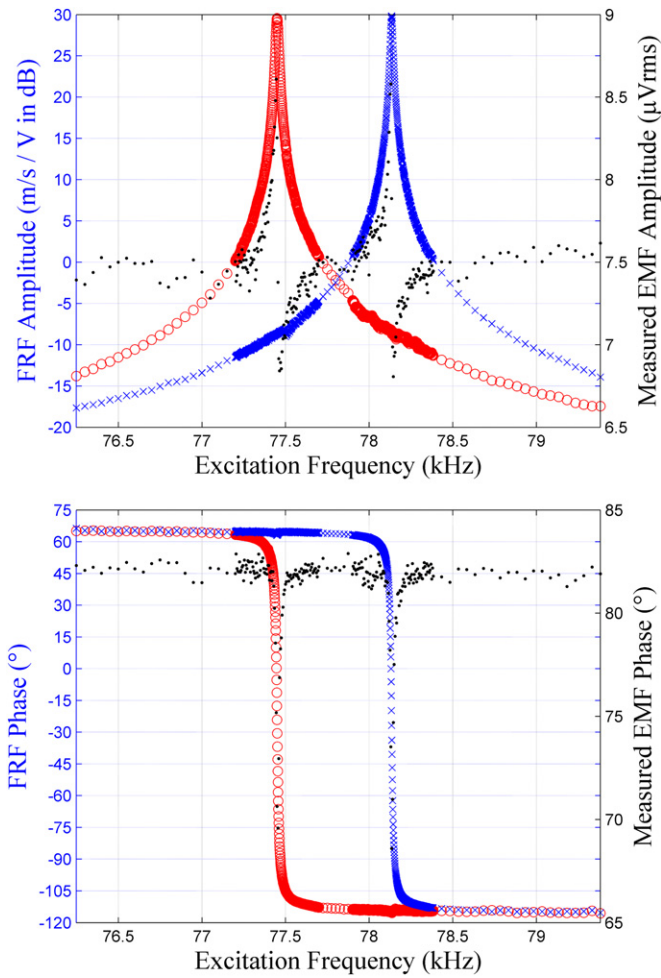


Figure 11. Experimentally-recovered amplitude and phase responses of the device obtained at 75 μ Torr using the reverse polarity configuration when the excitation voltage was 20 mVpp. The data shown in red (circles) and blue (crosses) are the mechanical responses of the left and right microcantilevers, respectively, while the response in black (dots) is the electrical response. Note the in the electrical amplitude response, antiresonances and response bias exist, while in the electrical phase response, non-resonant responses are dominated by inductive and resistive coupling effects.

and measurement system that is capable of resolving small changes in amplitude and phase over a small frequency range. In addition to the parasitic coupling effects that were observed at low-pressure testing, relatively larger excitations are needed to produce repeatable responses. This last effect is related to the noise characteristics of the particular excitation and measurement systems used. Thus, it is recommended that in future designs, the actuation wire trace should be designed for improved power handling, the sensing wire trace should be coiled to increase the signal return due to array vibrations, the relative geometry of the wire traces and contact pads should be optimized for minimal resistive coupling, and if possible the device should be wire bonded to reduce inductive coupling effects. Methods related to feedthrough cancellation might also be employed to mitigate issues related to inductive and resistive coupling [37–39]. Provided these alterations to the array’s design yield the previously-stated improvements, a lock-in amplifier might not be needed, which would enabling

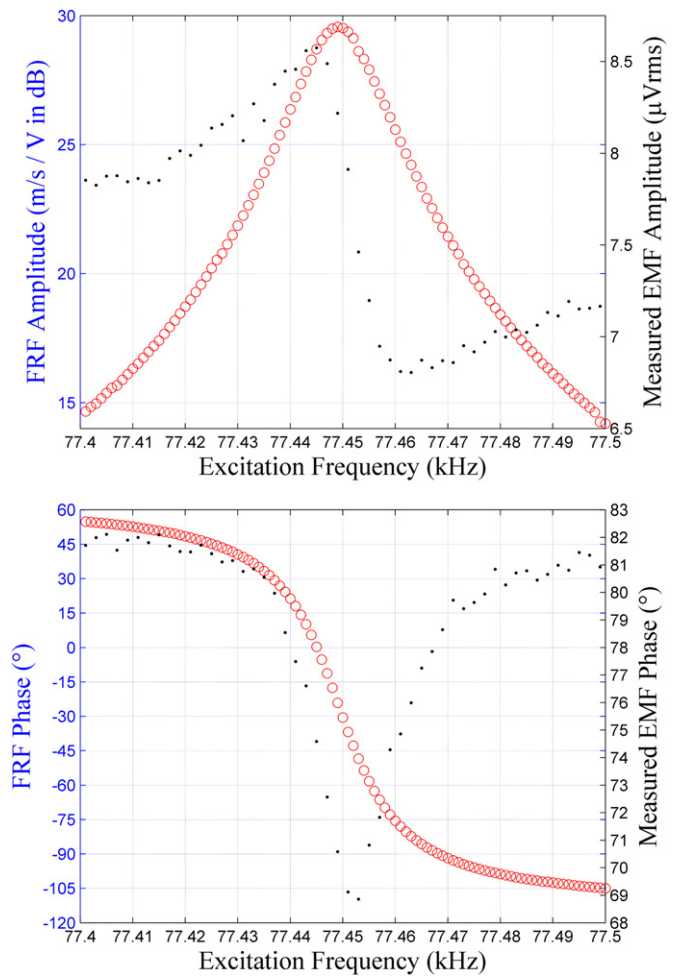


Figure 12. Experimentally-recovered amplitude and phase responses collected under the same conditions as in figure 11, except using smaller frequency increments. Note that the same effects related to inductive and resistive coupling depicted in figure 11 are present here, with the addition that the mechanical and electrical resonant frequencies are distinct due to these coupling issues.

the measurement of microcantilevers with higher natural frequencies and an overall more compact system.

The average power consumption metrics associated with the low-pressure and atmospheric-pressure results presented in this section were approximately 0.2 μ W and 5 μ W, respectively. Because of this, effects related to Joule heating are believed to be largely insignificant. However, this might not be true with a fully-integrated device, as it is expected that the majority of power consumed by the fully-integrated device will stem from attendant electronics. Accordingly, these electronics would need to be designed to consume minimal power and produce minimal heat to ensure that they do not significantly degrade the performance of the array.

3.1. Parametric identification

In order to validate the various assumptions needed to design the SISO electromagnetically-transduced microresonator array presented in this work, and to demonstrate how one might track multiple resonances with the electrical response of this array, this subsection describes a method capable of estimating

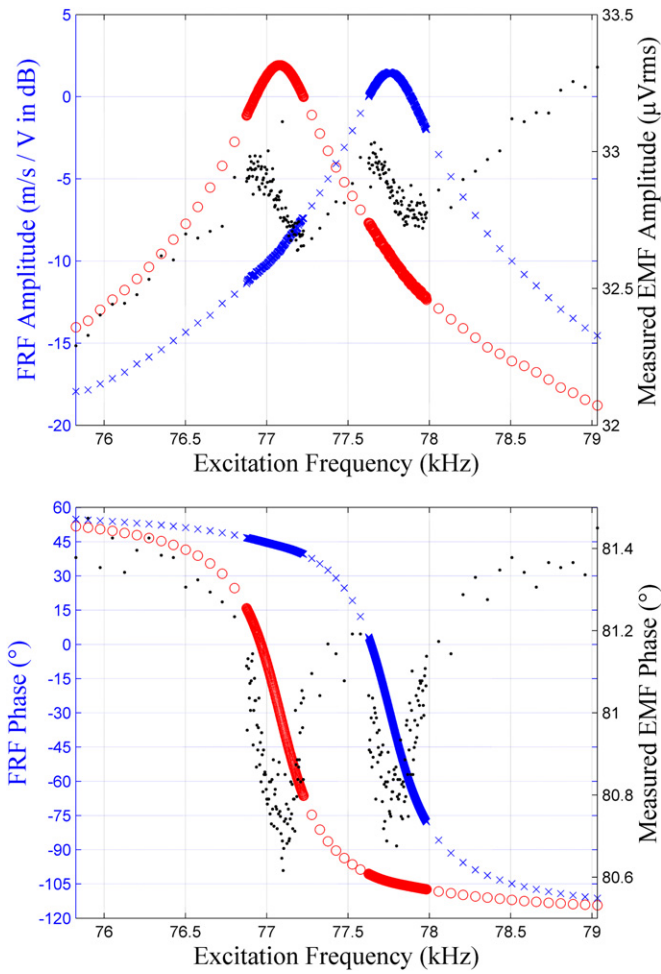


Figure 13. Experimentally-recovered amplitude response of the device obtained at 746 Torr using the reverse polarity configuration when the excitation voltage was 100 mVpp. Due to a decrease in the quality factors at atmospheric pressure as compared to low-pressure testing, the relative magnitude of the measured EMF due to the vibration of the array is decreased. Even though the electrical response due to mechanical vibrations is small near a mechanical resonance, the excitation and measurement system was capable of resolving the changes in the response due to array vibrations. Thus, even in the presence of inductive and resistive coupling, this device can still be used to detect shifts in the mechanical resonances of the microcantilevers at atmospheric pressure.

model parameters. In addition to identifying parameters, such as the natural frequencies of the microcantilevers, which are easily measured provided proper equipment, the adopted approach also estimates values that are considerably more difficult to measure directly, including the thickness of the microcantilevers or the strength of the local magnetic field.

In this work, a nonlinear least-squares method was employed [52], where the estimated parameters are defined to be the ones that minimize an error function that is the squared difference between the model and the measured response. In particular, the error function used was

$$E(\vec{p}) = \sum_{n=1}^M (a_n - a_n^*)^2 + (\phi_n - \phi_n^*)^2, \quad (27)$$

Table 2. A table of the bounds for the initial parameter estimates used by the PSO algorithm.

Parameter estimate bounds	Value
Length of beam 1 (l_1)	175–200 μm
Length of beam 2 (l_2)	175–190 μm
Thickness (v_0)	1.85–2.15 μm
Quality factor 1 at 75 μTorr (Q_1)	2418.35–6375.65
Quality factor 2 at 75 μTorr (Q_2)	2638.35–6955.65
Quality factor 1 at atmospheric pressure (Q_1)	111.1–292.9
Quality factor 2 at atmospheric pressure (Q_2)	104.5–275.5
Magnetic field strength ($B \sin \alpha$)	0.066–0.174 T
Lumped substrate resistance (R_{Si})	275–725 $\text{k}\Omega$
Mutual inductance (M)	0.176–0.464 μH

where \vec{p} is a vector containing the parameters of the model, M is the number of measurements, a_n and ϕ_n denote the amplitude and phase predicted by the model, and the superscript * is used to denote a measured value. Note that this model is only capable of uniquely estimating certain parameters, thus the values for mass density, modulus of elasticity, Au/Cr trace resistance, and microcantilever width provided in table 1 are assumed to be known values. The to-be-determined parameters are the lengths of the microcantilevers, the thickness of the microcantilevers, the respective quality factors for these microresonators, the component of the local magnetic field in the \mathbf{i} direction (see figure 2 for the orientation of the magnetic field), the lumped substrate resistance, and the mutual inductance. Note that the direction of the magnetic field, or the sign of the component of the local magnetic field used for sensing, cannot be determined using this method, due to its quadratic influence on the measured response.

One of the challenges with nonlinear least-squares methods is providing initial estimates for the parameters. To do this, a global minimization method called particle swarm optimization (PSO), previously implemented in [53], was used. Using a swarm of 5000 particles, a search space constrained by the limits provided in table 2 was used. Note that, in general, the bounds for the parameters are within 45% of a set of parameters that yielded a close fit to the data. The constraints for the lengths, however, are based on approximate measurements of the micrograph in figure 9. The bounds for the device layer thickness given by the manufacturer of the SOI wafer was $\pm 0.5 \mu\text{m}$. Based on measurements with a profilometer conducted during fabrication, and how the bounds for microcantilever thickness are coupled to the bounds for the lengths of the microcantilevers via the natural frequencies of these structures, bounds of $\pm 0.15 \mu\text{m}$ seemed more reasonable. In addition, a nonlinear constraint that the estimated parameters must yield natural frequencies within 100 Hz of the estimated values given in the previous section was used to mitigate the effects of poor estimates for the lengths and thickness of the microcantilevers. Satisfactory convergence for this method was determined when no change in the error function occurred after 50 iterations.

After estimates for parameters were found using PSO for the trials conducted at 75 μTorr and atmospheric pressure, these values were used as initial estimates to a nonlinear least-squares estimation algorithm implemented by

Table 3. Estimated values for the parameters for the trial conducted at 75 μ Torr.

Parameter estimates from 75 μ Torr trials	Value
Length of beam 1 (l_1)	$190.40 \pm 0.05 \mu\text{m}$
Length of beam 2 (l_2)	$189.56 \pm 0.05 \mu\text{m}$
Natural frequency 1 (f_1)	$77.4508 \pm 0.0002 \text{ kHz}$
Natural frequency 2 (f_2)	$78.1337 \pm 0.0002 \text{ kHz}$
Thickness (v_0)	$2.104 \pm 0.001 \mu\text{m}$
Quality factor 1 (Q_1)	4323.2 ± 0.2
Quality factor 2 (Q_2)	4470.1 ± 0.2
Magnetic field strength ($B \sin \alpha$)	$0.139 \pm 0.001 \text{ T}$
Lumped substrate resistance (R_{Si})	$456 \pm 2 \text{ k}\Omega$
Mutual inductance (M)	$0.3214 \pm 0.0009 \mu\text{H}$

Table 4. Estimated values for the parameters for the trial conducted at 746 Torr.

Parameter estimates from atmospheric pressure trials	Value
Length of beam 1 (l_1)	$200 \pm 800 \mu\text{m}$
Length of beam 2 (l_2)	$200 \pm 800 \mu\text{m}$
Natural frequency 1 (f_1)	$77.068 \pm 0.007 \text{ kHz}$
Natural frequency 2 (f_2)	$77.765 \pm 0.009 \text{ kHz}$
Thickness (v_0)	$2 \pm 10 \mu\text{m}$
Quality factor 1 (Q_1)	180 ± 10
Quality factor 2 (Q_2)	170 ± 9
Magnetic field strength ($B \sin \alpha$)	$0.1 \pm 0.9 \text{ T}$
Lumped substrate resistance (R_{Si})	$486 \pm 1 \text{ k}\Omega$
Mutual inductance (M)	$0.28284 \pm 0.00008 \mu\text{H}$

MATLAB's *lsqnonlin* function. This algorithm outputs not only the estimated parameters, as given in tables 3 and 4 for trials conducted in high vacuum and atmospheric pressure, respectively, but also residuals, or the differences between the model and measured values, and the Jacobian of the model with respect to the estimated parameters. These residuals and Jacobians are useful, as they can be used to determine the confidence intervals associated with the estimated parameters. Using MATLAB's *nparci* algorithm, 95% confidence intervals for the estimated parameters were found, and the half-widths of these intervals correspond to the error bounds on the values given in the tables. Note that since this estimation method does not directly calculate the natural frequencies of the microcantilevers, the model was reparameterized such that it depended on these values. The same methods were then used to estimate the other parameters, and their corresponding error bounds were used to estimate the frequencies.

It is important to highlight that while the adopted parametric identification technique is capable of estimating the variability of the parameters that were assumed to be unknown, it is not capable of estimating the variability of the parameters that were assumed to be known. This results from limitations of both the employed least-squares estimation technique and the experimental setup. While optical methods were used to confirm that the actual and nominal values for the widths of the microcantilevers were similar in magnitude, and similarly a multimeter was used to estimate the Au/Cr trace resistance, no tests were conducted to directly estimate the mass density or modulus of elasticity. Thus, the accuracy and validity of

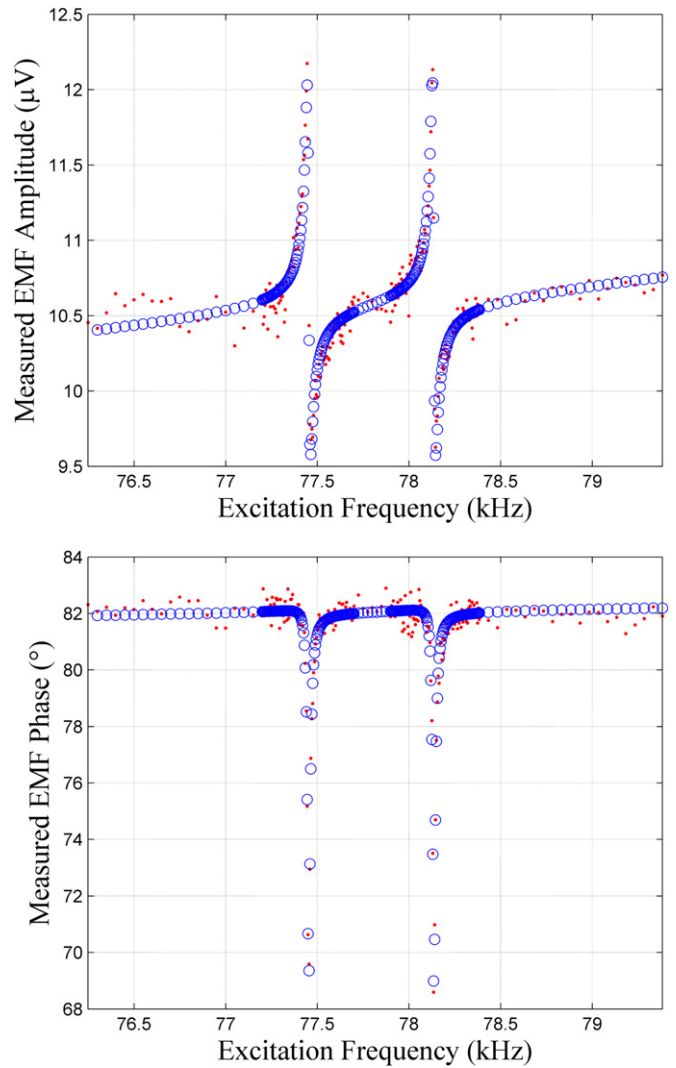


Figure 14. Overlays of the measured and modeled amplitude and phase response corresponding to trials conducted at 75 μ Torr. Measured and modeled values are denoted in red (dots) and blue (circles), respectively.

the estimated parameters are contingent on the accuracy and stationarity of the parameters that were assumed to be known.

Figures 14 and 15 depict overlays of the measured and modeled responses using the parameters obtained herein. Overall, both predictions describe the data fairly well. More importantly, the parameter estimates given in tables 3 and 4 provide validation for the model derived in this work. As referenced at the beginning of this subsection, estimates for parameters that are difficult to directly measure, like the thickness of the microcantilevers and the strength of the local magnetic field, are provided and are reasonable based on the nominal values provided by the manufactures. In addition, while under ideal circumstances, one might be able to directly measure the lengths of the microcantilevers using optical methods, this was not possible with the array used in this work due to residual silicon dioxide changing the effective lengths of these structures. Using the parameter estimation method described in this subsection, estimates for these lengths were found, and they appear to be reasonable based on inspection of the micrograph included in figure 9.

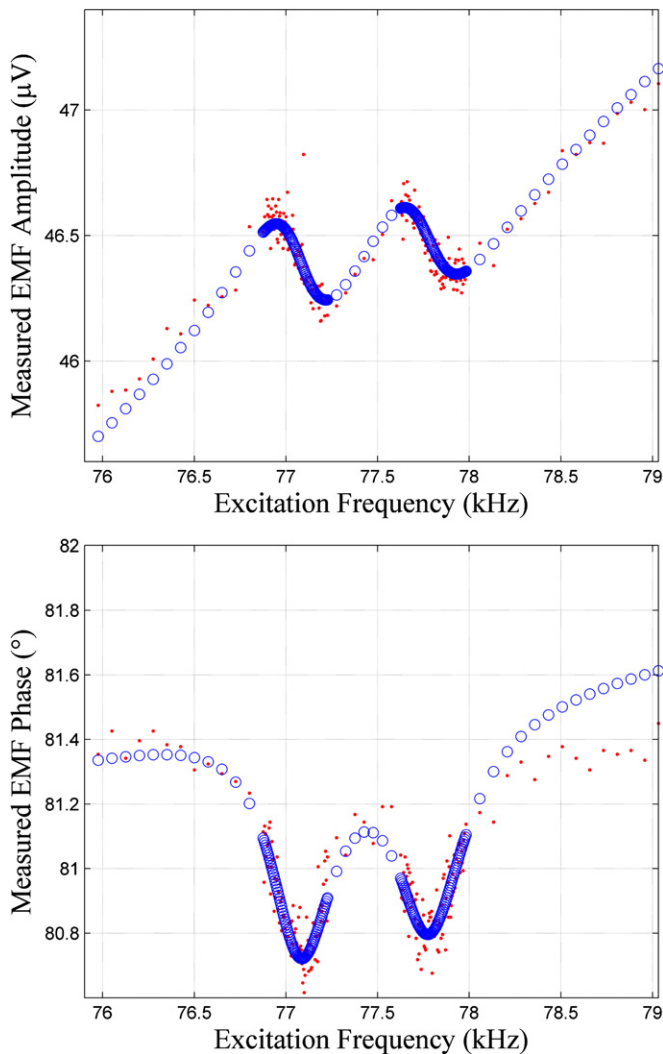


Figure 15. Overlays of the measured and modeled amplitude and phase response corresponding to trials conducted at 746 Torr. As in figure 14, measured and modeled values are denoted in red (dots) and blue (circles), respectively.

One important issue with the method presented here is that the parameter estimates that influence the mechanical dynamics of the array are sensitive to how strongly damped the microcantilevers are. That is, the error bounds for the parameters that influence the mechanical response that correspond to the high vacuum trial, and in turn a low-damping environment, are smaller than the same parameters corresponding to the atmospheric pressure trial, or a high-damping environment. Despite these issues, and the previously-discussed effects with inductive and resistive coupling altering the measured response, even at atmospheric pressure it is still possible to detect small changes in the natural frequencies of the microcantilevers, as the percent error of the measured values is approximately 0.01%.

4. Conclusions and future directions

In this work, a SISO electromagnetically-transduced microresonator array with multiple, easily-tailored resonances

was presented. The device was tested in low- and atmospheric-pressure environments, demonstrating the feasibility of operating this device in ambient conditions. A direct application of this research is resonant-based sensors that require only a single source and measurement system to track multiple resonances, but with a few simple modifications, these arrays could be used in tunable oscillators and in frequency multiplexing operations. The utilized distinct form of electromagnetic transduction suffers from intrinsic parasitic coupling between the input and output due to inductive and resistive effects, though methods related to feedthrough cancellation could be used to mitigate this issue. It is believed that much of the mutual inductance is due to the probe station, thus wire bonding the device should reduce much of these effects. In addition, redesigning the wire traces should also enable a reduction in the resistive coupling effects, improve power handling and increase signal return. Future work will focus on improving the design of this device and implementing larger arrays, making further progress towards a device with improved throughput.

Acknowledgments

This material is based in part upon work supported by the National Science Foundation under grant no. 0846385. Any opinions, findings, and conclusions or recommendations expressed in this material are those of the authors and do not necessarily reflect the views of the National Science Foundation. In addition, this work would not have been possible without the efforts of Drs V Kumar and A Mahmood, as well as ND Sheth.

References

- [1] Senturia S D 2000 *Microsystem Design* (Norwell: Kluwer)
- [2] Liu C 2006 *Foundations of MEMS* (Upper Saddle River: Prentice-Hall)
- [3] Nguyen C T-C and Howe R 1999 An integrated CMOS micromechanical resonator high-Q oscillator *IEEE J. Solid-State Circuits* **34** 440–55
- [4] Nguyen C T-C 2007 MEMS technology for timing and frequency control *IEEE Trans. Ultrason. Ferroelectr. Freq. Control* **54** 251–70
- [5] Salvia J, Melamud R, Chandorkar S, Lord S and Kenny T 2010 Real-time temperature compensation of MEMS oscillators using an integrated micro-oven and a phase-locked loop *J. Microelectromech. Syst.* **19** 192–201
- [6] Lutz M, Partridge A, Gupta P, Buchan N, Klaassen E, McDonald J and Petersen K 2007 MEMS Oscillators for high volume commercial applications *IEEE Solid-State Sensors, Actuators and Microsystems Conf.* pp 49–52
- [7] Greywall D S and Busch P A 2002 Coupled micromechanical drumhead resonators with practical application as electromechanical bandpass filters *J. Micromech. Microeng.* **12** 925–38
- [8] Demirci M U and Nguyen C T-C 2006 Mechanically corner-coupled square microresonator array for reduced series motional resistance *J. Microelectromech. Syst.* **15** 1419–36
- [9] Chivukula V B and Rhoads J F 2010 Microelectromechanical bandpass filters based on cyclic coupling architectures *J. Sound Vib.* **329** 4313–32

- [10] Pakdast H and Lazzarino M 2012 Triple coupled cantilever systems for mass detection and localization *Sensors Actuators A* **175** 127–31
- [11] Spletzer M, Raman A, Wu A Q, Xu X and Reifengerger R 2006 Ultrasensitive mass sensing using mode localization in coupled microcantilevers *Appl. Phys. Lett.* **88** 254102
- [12] DeMartini B E, Rhoads J F, Shaw S W and Turner K L 2007 A single input-single output mass sensor based on a coupled array of microresonators *Sensors Actuators A* **137** 147–56
- [13] DeMartini B E, Rhoads J F, Zielke M A, Owen K G, Shaw S W and Turner K L 2008 A single input-single output coupled microresonator array for the detection and identification of multiple analytes *Appl. Phys. Lett.* **93** 054102
- [14] Wang D, Chatani K, Ikehara T and Maeda R 2012 Mode localization analysis and characterization in a 5-beam array of coupled nearly identical micromechanical resonators for ultra-sensitive mass detection and analyte identification *Microsyst. Technol.* **18** 1–7
- [15] Bucher I, Avivi G and Velger M 2004 Design and analysis of multi degrees of freedom micro-mirror for triangular-wave scanning *Smart Struct. Mater.* **5390** 410–20
- [16] Elka A and Bucher I 2008 On the synthesis of micro-electromechanical filters using structural dynamics *J. Micromech. Microeng.* **18** 125018
- [17] Hodges C H 1982 Confinement of vibration by structural irregularity *J. Sound Vib.* **82** 411–24
- [18] Pierre C and Dowell E H 1987 Localization of vibrations by structural irregularity *J. Sound Vib.* **114** 549–64
- [19] Bouzit D and Pierre C 1995 An experimental investigation of vibration localization in disordered multi-span beams *J. Sound Vib.* **187** 649–69
- [20] Judge J A, Houston B H, Photiadis D M and Herdic P C 2005 Effects of disorder in one- and two-dimensional micromechanical resonator arrays for filtering *J. Sound Vib.* **290** 1119–40
- [21] Weinstein D, Bhawe S A, Tada M, Mitarai S, Morita S and Ikeda K 2007 Mechanical coupling of 2D resonator arrays for MEMS filter applications *IEEE Int. Frequency Control Symp.* pp 1362–5
- [22] Erbes A, Thiruvengathanathan P and Seshia A 2012 Impact of mode localization on the motional resistance of coupled MEMS resonators *IEEE Int. Frequency Control Symp.* pp 1–6
- [23] Abdelmoneum M A, Demirci M M, Li S-S and Nguyen C T-C 2004 Post-fabrication laser trimming of micromechanical filters *IEEE Int. Electron Devices Meeting* pp 39–42
- [24] Paci D, Pieri F, Toscano P and Nannini A 2008 A CMOS-compatible, magnetically actuated resonator for mass sensing applications *Sensors Actuators B* **129** 10–17
- [25] Manginell R P et al 2008 Mass-sensitive microfabricated chemical preconcentrator *J. Microelectromech. Syst.* **17** 1396–407
- [26] Sabater A B, Kumar V, Mahmood A and Rhoads J F 2013 On the nonlinear dynamics of electromagnetically-transduced microresonators *J. Microelectromech. Syst.* **22** 1020–31
- [27] Lang H P, Hegner M and Gerber C 2005 Cantilever array sensors *Mater. Today* **8** 30–36
- [28] Villarroya M et al 2006 System on chip mass sensor based on polysilicon cantilevers arrays for multiple detection *Sensors Actuators A* **132** 154–64
- [29] Truitt P A, Hertzberg J B, Huang C C, Ekinici K L and Schwab K C 2007 Effective and sensitive capacitive readout of nanomechanical resonator arrays *Nano Lett.* **7** 120–6
- [30] Venstra W and van der Zant H S J 2008 Efficient readout of micromechanical resonator arrays in ambient conditions *Appl. Phys. Lett.* **93** 234106
- [31] Guan S 2003 Frequency encoding of resonant mass sensors for chemical vapor detection *Anal. Chem.* **75** 4551–7
- [32] Basarir O, Bramhavar S and Ekinici K L 2012 Motion transduction in nanoelectromechanical systems (NEMS) arrays using near-field optomechanical coupling *Nano Lett.* **12** 534–9
- [33] Jackson J D 1962 *Classical Electrodynamics* (New York: Wiley)
- [34] Long J R 2000 Monolithic transformers for silicon RF IC design *IEEE J. Solid-State Circuits* **35** 1368–82
- [35] Fong N, Plouchart J-O, Zamdmer N, Kim J, Jenkins K, Plett C and Tarr G 2003 High-performance and area-efficient stacked transformers for RF CMOS integrated circuits *IEEE MTT-S Int. Microwave Symp.* pp 967–70
- [36] Clark J, Hsu W-T, Abdelmoneum M and Nguyen C T-C 2005 High-Q UHF micromechanical radial-contour mode disk resonators *J. Microelectromech. Syst.* **14** 1298–310
- [37] Lee J E-Y, Zhu Y and Seshia A A 2008 A bulk acoustic mode single-crystal silicon microresonator with a high-quality factor *J. Micromech. Microeng.* **18** 064001
- [38] Xu Y and Lee J 2012 Single-device and on-chip feedthrough cancellation for hybrid MEMS resonators *IEEE Trans. Indust. Electron.* **59** 4930–7
- [39] Tang M, Cagliani A, Escoufflaire M, Mouisel S and Davis Z 2010 Noise depression of parasitic capacitance for frequency detection of micromechanical bulk disk resonator *IEEE Int. Conf. on Nano/Micro Engineered and Molecular Systems* pp 728–31
- [40] Sazonova V, Yaish Y, Ustunel H, Roundy D, Arias T A and McEuen P L 2004 A tunable carbon nanotube electromechanical oscillator *Nature* **431** 284–7
- [41] Lassagne B, Garcia-Sanchez D, Aguasca A and Bachtold A 2008 Ultrasensitive mass sensing with a nanotube electromechanical resonator *Nano Lett.* **8** 3735–8
- [42] Arnold D P and Wang N 2009 Permanent magnets for MEMS *J. Microelectromech. Syst.* **18** 1255–66
- [43] Rozenberg Y I, Rosenberg Y, Krylov V, Belitsky G and Shacham-Diamand Y 2006 Resin-bonded permanent magnetic films with out-of-plane magnetization for MEMS applications *J. Magn. Magn. Mater.* **305** 357–60
- [44] Wang N and Arnold D P 2010 Batch-fabricated electrodynamic microactuators with integrated micromagnets *IEEE Trans. Magn.* **46** 1798–801
- [45] Jiang Y, Fujita T, Uehara M, Iga Y, Hashimoto T, Hao X, Higuchi K and Maenaka K 2011 Fabrication of NdFeB microstructures using a silicon molding technique for NdFeB/Ta multilayered films and NdFeB magnetic powder *J. Magn. Magn. Mater.* **323** 2696–700
- [46] Sun X M, Yuan Q, Fang D M and Zhang H X 2011 Electrodeposition and characterization of CoNiMnP-based permanent magnetic film for MEMS applications *IEEE Nano/Micro Engineered and Molecular Systems Conf.* pp 367–71
- [47] Chao T Y, Lin J R and Cheng Y T 2012 CoNiMnP-AAO hard magnetic nanocomposite film for MEMS applications *IEEE Nano/Micro Engineered and Molecular Systems Conf.* pp 351–4
- [48] Ramadan Q, Samper V D, Puiu D P and Yu C 2006 Fabrication of three-dimensional magnetic microdevices with embedded microcoils for magnetic potential concentration *J. Microelectromech. Syst.* **15** 624–38
- [49] Badilita V, Kratt K, Burger T, Korvink J G and Wallrabe U 2009 3D high aspect ratio, MEMS integrated micro-solenoids and Helmholtz micro-coils *IEEE Solid-State Sensors, Actuators and Microsystems Conf.* pp 1106–9

- [50] Glickman M, Tseng P, Harrison J, Goldberg I B, Johnson P, Smeys P, Niblock T and Judy J W 2009 CMOS-compatible back-end process for in-place actuating ferromagnetic MEMS *IEEE Solid-State Sensors, Actuators and Microsystems Conf.* pp 248–51
- [51] Li H Y, Xie L, Ong L G, Baram A, Herer I, Hirshberg A, Chong S C, Gao S and Kwong D L 2012 Three-dimensional solenoids realized via high-density deep coil stacking for MEMS application *IEEE Electron Device Lett.* [33](#) 432–4
- [52] Seber G A F and Wild C J 1989 *Nonlinear Regression* (New York: Wiley)
- [53] Chen S 2013 Another particle swarm toolbox *MATLAB Central File Exchange*